Cairo University

Journal of Advanced Research

ORIGINAL ARTICLE

Effect of strontium on Nd doped $Ba_{1-x}Sr_xCe_{0.65}Zr_{0.25}Nd_{0.1}O_{3-\delta}$ proton conductor as an electrolyte for solid oxide fuel cells

CrossMark

J. Madhuri Sailaja *, **K. Vijaya Babu**, **N. Murali**, **V. Veeraiah**

Department of Physics, Andhra University, Visakhapatnam, Andhra Pradesh, India

G R A P H I C A L   A B S T R A C T
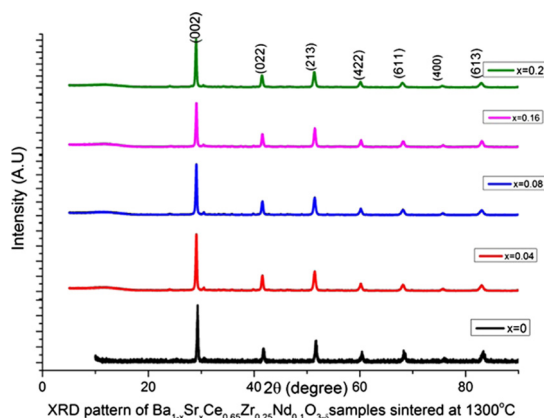
XRD pattern of $Ba_{1-x}Sr_xCe_{0.65}Zr_{0.25}Nd_{0.1}O_{3-\delta}$ samples sintered at 1300°C

A R T I C L E   I N F O

A B S T R A C T

This paper investigated the Sr doping effect on the microstructure, chemical stability, and conductivity of $Ba_{1-x}Sr_xCe_{0.65}Zr_{0.25}Nd_{0.1}O_{3-\delta}$ ($0 \leqslant x \leqslant 0.2$) electrolyte prepared by sol-gel method. The lattice constants and unit cell volumes were found to decrease as Sr atomic percentage increased in accordance with the Vegard law, confirming the formation of solid solution. Incor-

* Corresponding author.
E-mail address: madhurisailaja1981@gmail.com (J. Madhuri Sailaja).

poration of Sr into the composition resulted in smaller grains besides suppressing the formation of secondary phases of $SrCeO_3$. Among the synthesized samples $BaCe_{0.65}Zr_{0.25}Nd_{0.1}O_{3-\delta}$ pellet with orthorhombic structure showed highest conductivity with a value of 2.08×10^{-3} S/cm(dry air) and 2.12×10^{-3} S/cm (wet air with 3% relative humidity) at 500 °C due to its smaller lattice volume, larger grain size, and lower activation energy that led to excessive increase in conductivity. $Ba_{0.8}Sr_{0.2}Ce_{0.65}Zr_{0.25}Nd_{0.1}O_{3-\delta}$ recorded lower conductivity with a value of 4.62×10^{-4} S/cm (dry air) and 4.83×10^{-4} S/cm (wet air with 3% relative humidity) at 500 °C than Sr undoped but exhibited better chemical stability when exposed to air and H_2O atmospheres. Comparisons with the literature showed the importance of the synthesis method on the properties of the powders. Hence this composition can be a promising electrolyte if all the values such as sintering temperature, Sr dopant concentration, and time are proportionally controlled.

Introduction

Compounds based on alkali earth metal cerates such as barium cerate and strontium cerate with perovskite structures are potential materials for their applications in fuel cells such as electrolytes, selective ceramic membrane reactors, electro catalysts having high ionic conductivity, and steam sensor at elevated temperatures [1–12]. The design of such electrochemical devices requires materials with desirable properties such as high protonic or mixed ionic electronic conductivity, mechanical strength, and thermal compatibility. Nevertheless, materials for proton conducting membranes are yet to emerge effectively. Therefore extensive researches in the fields of proton absorption and migration mechanisms, as well as further application tests are required. Several researchers have synthesized $BaCeO_3$ using various methods such as solid state method, sol-gel, and auto combustion [13–15] but the problem is when exposed to CO_2 containing atmosphere, the material decomposed into barium carbonate and cerium oxide and thus found unstable. In contrast to $BaCeO_3$, $BaZrO_3$ is chemically more stable in CO_2 containing atmospheres but has low proton conductivity [16,17]. Materials synthesized by conventional solid state method have the disadvantage that the oxides and carbonates need calcination temperatures $\geqslant 1200$ °C followed by a sintering temperatures $\geqslant 1400$ °C. Such prolonged calcinations may result in crystal growth which hinders the formation of dense ceramics although they possess good electrical properties. To overcome these problems wet chemical method is used for the preparation of the powders which resulted in better homogeneity coupled with improved reactivity and dense particles with smaller particle size at lower sintering temperatures [18].

Co-doping strategy in $BaCeO_3$ as observed from the literature evolved in a convoluted impact on the transport properties. From the investigations of Su et al. [19], higher conductivity was detected at $x = 0.15$ for the composition $BaCe_{0.8}Y_xNd_{0.2-x}O_{3-\delta}$. Lee et al. [20] analysed the influence of Y^{3+} and Nd^{3+} concentrations on the transport properties of $BaCe_{0.8}Y_xNd_{0.2-x}O_3$ obtained by mechanical ball milling method which outlined that with a rise in x, the conductivity depicted a hike. This counterstatement may be attributed to the difference in the microstructure of the material and the preparation techniques. Fu et al. [21] synthesized $BaCe_{0.85}Y_{0.1}Nd_{0.05}O_{3-\delta}$ electrolyte in which the power density of the material displayed 173×10^6 W/cm² (923 K). Also Zhang and Zhao [22] reported that by doping strontium in $Ba_{1-x}Sr_xCe_{0.9}Nd_{0.1}O_{3-\delta}$, the oxygen ion contribution to the total conductivity dropped from 7×10^{-2} to 4×10^{-2} mS/cm (hydrogen atmosphere at 873 K) from $x = 0$ to 0.2. Iwahara [23] developed an Nernstian hydrogen sensor using $BaCe_{0.9}Nd_{0.1}O_{3-\delta}$ as an electrolyte at 200–900 °C under several concentrations of H_2 in argon ($pH_2 = 10^4$–1 atm) and the response time of the cell Pt$BaCe_{0.9}Nd_{0.1}O_{3-\delta}$ Pt was approximately 120 s (723 K). Also Cai et al. [24] interpreted the hydrogen permeation flux i.e. 0.02 mL (STP) at 1273 K under H_2/He gradients for $BaCe_{0.95}Nd_{0.05}O_{3-\delta}$. Also characteristics of $BaZr_{0.4}Ce_{0.4}In_{0.2}O_{3-\delta}$ ceramics were studied as an electrolyte which in turn manifested good sensing properties in a reducing atmosphere [25]. Recent reports have manifested that Zr substituted, Nd doped barium cerate maintained good conductivity in air up to compositions of 40% Zr on the Ce site [26].

Neodymium Nd (III), an aliovalent cation of rare earth element is selected as a dopant because of its deteriorating tendency for partitioning into A-site positions; however, it is not fully identified in $BaCeO_3$-$BaZrO_3$ solutions. Analysis in this work was based on the parameters such as cell volume, tolerance factor, and electro negativities of A and B site atoms. In terms of thermodynamics, $SrCeO_3$ is more stable than $BaCeO_3$ and as on date very few research papers dealt with $BaSrCeZrO_3$ structures. Thus the present work was aimed to investigate the effect of strontium by partially replacing Ba in the A sites in Nd doped barium cerate- zirconates and examines the chemical stability and conductivity.

Experimental

Powder preparation

The citrate-EDTA complexing sol-gel process is used for preparing $Ba_{1-x}Sr_xCe_{0.65}Zr_{0.25}Nd_{0.1}O_3$ ($x = 0$, 0.04, 0.08, 0.16, 0.2) oxides. The starting materials were commercial $Ba(NO_3)_2$ (Sigma Aldrich 99.9%, Andhra Pradesh, India), $ZrO(NO_3)_2 \cdot 2H_2O$ (High Media, 99.5%, Andhra Pradesh, India), $Ce(NO_3)_3 \cdot 6H_2O$ (High Media, 99.5%, Andhra Pradesh India), $Sr(NO_3)_2$, $Nd(NO_3)_3 \cdot 6H_2O$ (Sigma Aldrich 99.9%, Andhra Pradesh India). Both citric acid (Sigma Aldrich 99.9%, Andhra Pradesh, India) and EDTA (Sigma Aldrich 99.9%, Andhra Pradesh, India) perform the operation of chelating agents to the precursor solution. The ratio of molar solutions of EDTA: citric acid: Total metal cations content is set at 1:2:1. The pH value of the solution is adjusted to be ~6 by adding small amounts of NH_4OH (Sigma Aldrich, 99.98%, Andhra Pradesh, India). The mixed solutions were heated to

100 °C under continuous stirring (Remi magnetic stirrer with hot plate model 2 mLH, power 300 W, Visakhapatnam, India) over night to remove excess water and promote polymerization. During continuous heating, the solution became more viscous with a change of colour from colourless to dark brown gel form. When further heated to a temperature of 250 °C/24 h in an oven to evaporate residual water and organics, these gels get converted into black powders. The synthesized powders are now calcined at 1100 °C (12 h) with a heating rate of 5 °C/min. All the samples are coloured in chocolate brown which is marked in contrast to the yttrium doped materials of pale yellow in colour. To obtain dense samples, the resulted fine calcined powders were uniaxially pressed into cylindrical pellets at 5ton pressure and then sintered (at 1300 °C for 5 h at a heating rate of 5 °C min^{-1}) in air atmosphere. While sintering, a small amount of powder is sprinkled on the platinum foil to avoid material evaporation in the process.

Characterization

Thermo gravimetric analysis (TGA) is carried out to the dried powder (T = 250 °C) by a TA instrument (Thermal analyzer NETZSCH STAC449F3 Jupiter, IIT Madras, Chennai, India). The phase identification of the sintered oxides is analysed with a powder diffractometer (PANalytical X-pert Pro, Netherlands) with Ni filtered Cu-Kα radiation and the diffraction angle from 10° to 90° with an interval of 0.01°/min. Morphologies of the sintered pellets are examined using scanning electron microscope (JEOL model JSM-6610 LV) in combination with an energy dispersion spectrometer (EDS) (INCA Energy 250, Oxford, UK) to estimate the percentage of elements present in the samples. FTIR spectrometer (SHIMADZU IR Prestige-21, Singapore) is employed to record the Fourier transform infrared (FTIR) spectra of calcined and sintered $Ba_{1-x}Sr_xCe_{0.65}Zr_{0.25}Nd_{0.1}O_{3-\delta}$ powder in the range of 4000–400 cm^{-1} to investigate the complex, carbonates and oxides formation. The theoretical density of the powders is calculated with the obtained XRD. Fourier transforms Raman spectroscopy (BTC111-RAMAN-785, UK) studies are conducted to study the vibrational modes of the samples in the range 0–1200 cm^{-1}. LCR measurements from room temperature up to 500 °C (in dry air and wet air with 3% relative humidity) are performed (Wayne Kerr P65000 model LCR meter, India) in the frequency range from 20 Hz to 1 MHz. Silver paste (Alfa Aesar, Vishakhapatnam, India) is painted on both sides of the pellet and heated in a furnace at 375 °C for half an hour prior to Impedance measurements.

Results and discussion

Thermogravimetric/differential thermal analysis (TG-DTA)

To explore the reaction during the formation of the perovskite phase structure, simultaneous TG-DTA curves of the samples are conducted from room temperature to 1200 °C. In terms of thermal stability nitrates are unstable compared to carbonates; hence, they can be decomposed easily. Three regions are obtained in TG-DTA of the powder as shown in Fig. 1a–e. The gradual weight loss is 12–15% up to 100 °C and this is due to absorption of water molecules. The further weight loss accompanied by two exothermal peaks in DTA discloses that the decomposition of gel takes place in two steps. The weight loss from 100 °C to 500 °C was found to be 20–30% accompanied with small exothermic peak near 500–550 °C, which may be due to thermal decomposition of the citrate complex, burning of citrate chains and metal nitrates. The weight loss from 500–1000 °C and the exothermic peaks near 900 °C are due to co-oxidation. A very small weight loss was observed above 1000 °C, which is due to thermal decomposition of barium carbonate, with the release of CO_2 for all the samples [27–28]. This finding is consistent with the XRD results that $Ba_{1-x}Sr_x Ce_{0.65}Zr_{0.25}Nd_{0.1}O_{3-\delta}$ phase only forms upon calcined at 1000 °C and above. There is no noticeable weight change when the temperature was higher than 1100 °C, indicating the complete decomposition of $BaCO_3$ and formation of $BaSr_xCe_{0.65}Zr_{0.25}Nd_{0.1}O_{3-\delta}$ compound. A small amount of weight gain was observed for samples with x = 0, 0.04 and 0.08 above 1200 °C, which may be due to the formation of $BaCO_3$ or $SrCeO_3$ same as second phase, which are absent as the content of strontium increased. Individual decomposition of the compound with respect to heat treatment is illustrated below in Table 1.

XRD analysis

Fig. 2 shows the XRD patterns of calcined (1100 °C) and sintered (1300 °C) ceramic powders. It is evident from TG/DTA measurements that the complete decomposition of carbonates/nitrates needs 1100 °C and correspondingly the XRD patterns at 1100 °C confirm the single perovskite phase formation with very small $BaCeO_3$ and CeO_2 impurities. This can be attributed to altered synthesis procedure of Pechini method in which the pH was adjusted to 6 in contrast to the conventional wet chemical method combustion that maintains a low pH (∼1). With increase in the pH value to 6, more protons get released from citric acid to fasten the chelating process and help in the phase formation at a lower temperature [29].

The formation of $BaCO_3$ impurity may be due to the reaction between Ba^{2+} ions and CO_3^{2-} ions, which may be formed due to the reaction between citric acid and EDTA during heating [30]. Besides a small weak peak was identified in the calcined sample that may be attributed to CeO_2 like phase since the peaks are closer to the CeO standard data JCPDS (33-0334). As Sr doping is increased to 0.2 the CeO like second phase is hindered. Details of the lattice parameters and crystal structure are elucidated in Table 2.

All the sintered $Ba_{1-x}Sr_xCe_{0.65}Zr_{0.25}Nd_{0.1}O_{3-\delta}$ oxides displayed predominant orthorhombic perovskite structure with *Pmcn* space group and the peaks matched with the characteristic diffraction pattern of $BaCeO_3$ (JCPDS 22-0074) representing seven diffraction signals namely (0 0 2), (0 2 2), (2 1 3), (6 1 1), (4 2 2), (4 4 0), and (6 1 3) planes. The lattice parameters are calculated from the XRD analysis based on the standard data of $BaCeO_3$ and a linear relation between the lattice parameters and Sr doping content was noticed. The X-ray diffraction angles of $Ba_{1-x}Sr_xCe_{0.65}Zr_{0.25}Nd_{0.1}O_{3-\delta}$ perovskite shifted to higher angles with increase in the Sr doping content and are consistent with the investigations reported by Zeng
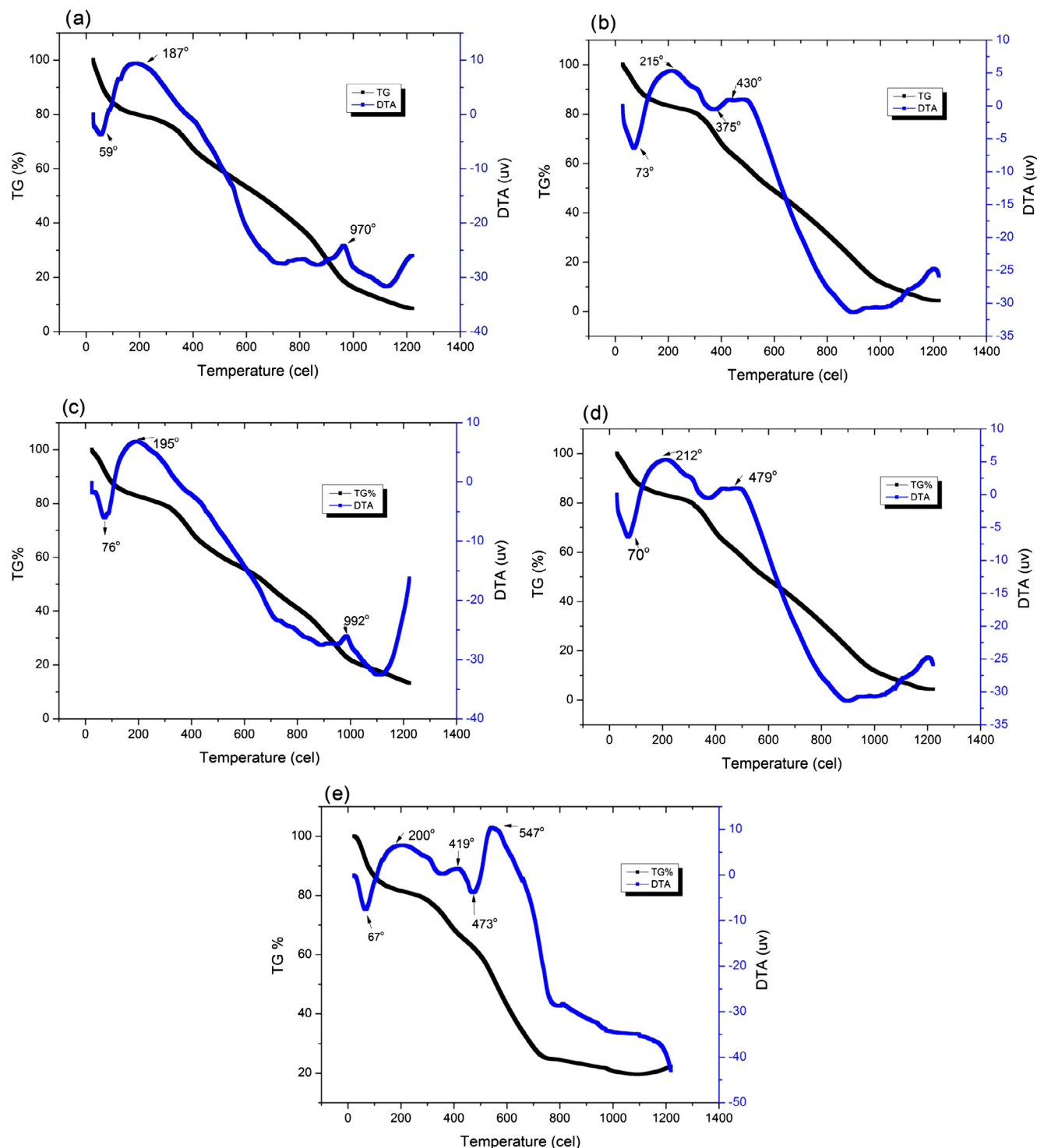
Fig. 1 Thermal analysis of $Ba_{1-x}Sr_xCe_{0.65}Zr_{0.25}Nd_{0.1}O_{3-\delta}$ samples heated at 250 °C for 24 h (a) $x = 0$, (b) $x = 0.04$, (c) $x = 0.08$, (d) $x = 0.16$, (e) $x = 0.2$.

et al. [31]. Due to the ionic differences of Sr^{2+} (1.18 Å) and Ba^{2+} (1.34 Å) ions at the A site of the perovskite, the lattice parameters and cell volumes of ceramics displayed a nearly decreasing trend owing to the increase in the Sr content, the finding which is in accordance with the Vegard law. The crystallite sizes of the powder were calculated using Scherrer's formula and a slight increase in the crystallite size was noticed from 29 nm (Sr = 0) to 31.3 nm (Sr = 0.2).

Chemical stability

Barium cerate structure is not chemically stable because it can react with CO_2 according to the reaction (1) or with H_2O according to reaction (2)
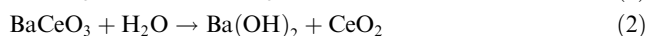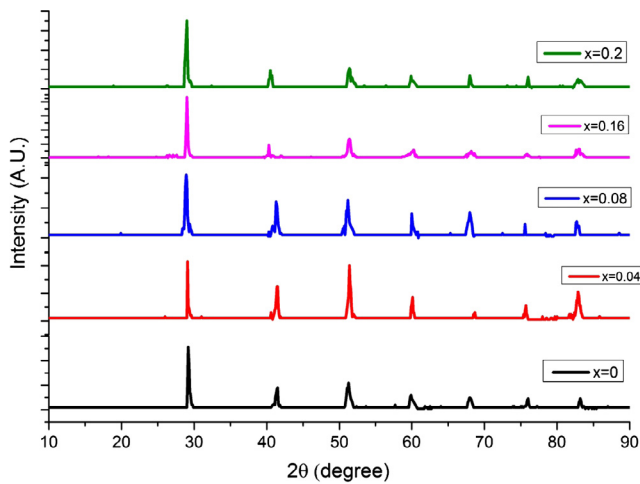
$$BaCeO_3 + CO_2 \rightarrow BaCO_3 + CeO_2 \tag{1}$$

$$BaCeO_3 + H_2O \rightarrow Ba(OH)_2 + CeO_2 \tag{2}$$

Table 1 The summarization of thermal characteristics for dried powders ($T = 250$ °C).

Sr content	Stage	Temperature (°C)	Mass loss (%)	Exothermic peak (°C)	Total mass Loss (%)
$X = 0$	1	30–120	15	187,970	83
	2	120–525	27		
	3	525–900	38		
$X = 0.04$	1	30–120	12		89
	2	120–645	40	215,430	
	3	640–1100	37		
$X = 0.08$	1	30–110	11		72
	2	110–600	31	195	
	3	600–950	30	992	
$X = 0.16$	1	30–120	10	212	79
	2	130–630	39	479	
	3	630–1100	33		
$X = 0.2$	1	30–110	11		84
	2	114–730	63	201,419,547	
	3	730–1100	10		

Fig. 2b XRD patterns of samples sintered at 1300 °C.

Fig. 2a XRD patterns of samples calcined at 1100 °C.

Fig. 2c XRD of samples exposed to boiling water.

Fig. 2d XRD patterns of samples exposed to CO_2.

In order to verify the stability under H_2O containing atmospheres, the sintered pellets are boiled in water for 2 h, dried, and the XRD patterns are recorded. It has been observed that after being exposed to boiling water, the $Ba_{1-x}Sr_xCe_{0.65}Zr_{0.25}Nd_{0.1}O_{3-\delta}$ pellets retained original perovskite structure with less additional peaks showing $BaCO_3$ phase as shown in Fig. 2c. Due to reaction with H_2O, $BaCO_3$ may also form due to interaction with atmospheric CO_2 that converts Ba $(OH)_2$ into carbonate. The reaction product CeO_2 that may appear is insoluble in water and forms a porous layer on the surface of the $BaCeO_3$ pellet while Ba $(OH)_2$ results in a substantial volume expansion thereby forming cracks on the surface [32]. Subsequently water penetrates into the material through the cracks on the surface, which resulted in further reaction with $BaCeO_3$. Among all the samples, the composition with $x = 0.16$ exhibited more chemical stability.

A neutron diffraction study shows that at room temperature and pressure, in the replacement of Zr with Ce, the size
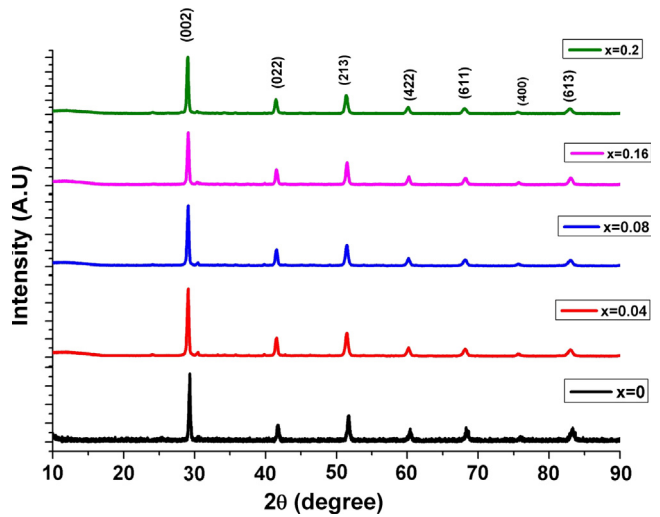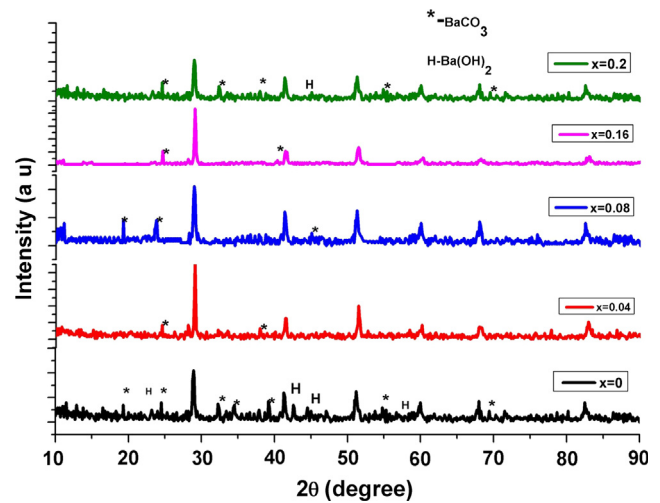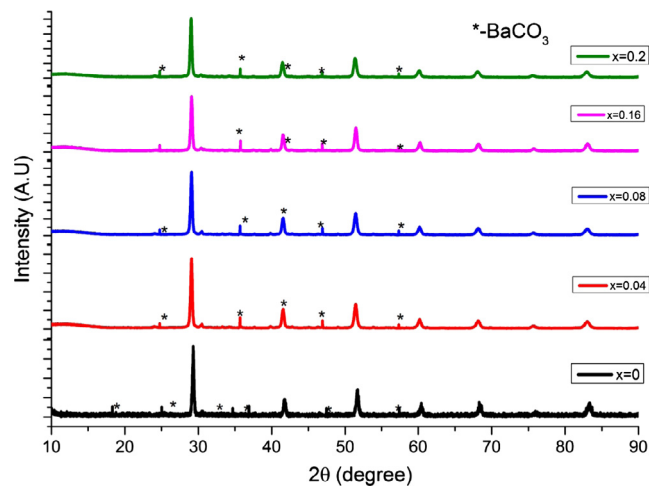
Table 2 Summary of crystal parameters and tolerance factor of sintered $Ba_{1-x}Sr_xCe_{0.65}Zr_{0.25}Nd_{0.1}O_{3-\delta}$ powders.

x	Crystal symmetry	a (Å)	b (Å)	c (Å)	Cell volume (Å)³	Relative density (%)	Tolerance factor (t)
0	Orthorhombic	8.64321	6.22356	6.23061	335.119	89	0.8667
0.04	Orthorhombic	8.68669	6.19147	6.15501	331.037	90	0.865
0.08	Orthorhombic	8.70340	6.15877	6.15081	329.697	90	0.863
0.16	Orthorhombic	8.69101	6.14509	6.14509	328.633	91	0.86
0.2	Orthorhombic	8.64483	6.11920	6.14570	325.858	90	0.856

of BO_6 octahedral decreases with increase in zirconium content as Zr acts as a phase stabilizer. Therefore the driving force for the evolution towards a symmetric structure was increased and it becomes more difficult to distort the perovskite structure. Also stability in water increases with decreasing ionic radius of the codopant [29,33], which confirms the present result. Incorporation of Sr further increased the stability of the compound as indicated by XRD.

To check the stability of the material against atmospheric CO_2, a small amount was left out in the laboratory for a period of 20 days and the XRD analysis did not show any phase change except for small peaks indicating $BaCO_3$ as shown in Fig. 2d. These results suggested that when strontium is doped in the A sites of barium cerates, it can undoubtedly improve the chemical stability of $Ba_{1-x}Sr_x$-$Ce_{0.65}Zr_{0.25}Nd_{0.1}O_{3-\delta}$ compound. It has been reported that the stability of the perovskite structures increases with increase in the tolerance factor [33], which is in line with the calculated tolerance factor and experimental lattice parameters of $Ba_{1-x}Sr_xCe_{0.65}Zr_{0.25}Nd_{0.1}O_{3-\delta}$ when compared to the undoped tolerance factor value of $BaCeO_3$. Matsumoto et al. investigated chemical stability of $BaCeO_3$-based proton conductors doping different trivalent cations with thermo gravimetry (TG) analysis and found that stability increases with reduction in ionic size of the dopant, which correlated with the present result [34]. The stability of Sr doped barium cerates in wet atmospheres is in agreement with the present result [35].

Scanning electron microscope and EDAX analysis

The morphological investigations of the sintered (1300 °C) powders confirmed that the modified pechini process favoured the formation of foamed structures with sub micro-metre particle (1.85–4.17 μm) of sintered $Ba_{1-x}Sr_xCe_{0.65}Zr_{0.25}Nd_{0.1}O_{3-\delta}$ pellet powders. The ceramic pellets are well densified although very few pores are observed, which may have resulted in the shrinkage of the volume of the synthesized pellet due to evaporation of the surface water and residual organics during high sintering temperatures. The powders prepared from citrate EDTA sol gel process resulted in a dense structure, which may be due to excess barium sprinkled on the platinum foil during sintering depending on the Sr content and it may have compensated to the amount of barium evaporation that resulted due to high heat treatment. From $x = 0.0$ to $x = 0.2$, a slight decrease in the grain size was observed as Sr doping increased.

In order to realize the effect of Sr doping on the structural stability, the distortion of cubic lattice was calculated based on the Goldsmith tolerance factor given by the formula:

$$\tau = \frac{r_a + r_o}{\sqrt{2}(r_b + r_o)} \quad (3)$$

where r_a, r_b and r_o are the ion radius of the A, B and oxygen sites respectively.

Perovskite structure can be formed only with the correct selection of A site cation: B site cation: Oxygen ion ratio as predicted by Goldsmith values of tolerance factor calculated and tabulated in Table 2. It was observed that barium atoms are too small to stabilize cubic perovskite structure with the given B site composition. Smaller Sr^{2+} when substituted into the lattice creates distortion of the crystal lattice and contributes to global lowering of symmetry of the lattice that is evident from the decrease in the tolerance factor and increase in the octahedron tilting angle. In such a deformed lattice, equilibrium sites for protons located near oxygen ions are separated by higher energy barriers than for isotropic, ideal cubic symmetry. As a result, protons become localized and macroscopic activation energy of conductivity which represents height of energy barrier increases amorously thus hindering conductivity [36].

The bulk densities of the sintered powders are calculated by the Archimedes displacement principle and theoretical density from XRD. The relative density of all the samples sintered at 1300 °C was found to be around 92% of the theoretical density and its value can be confirmed from the SEM images as shown in Fig. 3. Sintering at higher temperatures may further enhance the density but there may be a chance of more BaO evaporation. EDAX analysis confirmed that all the elements are present in stoichiometric ratio and no impurities are detected in the powders. The elemental analysis of the individual compounds is represented in Fig. 3.

Fourier transform infrared spectroscopy (FTIR)

Fig. 4 shows the FTIR Spectra of the sintered samples. The peaks near 860–869 cm^{-1} may be assigned to the metal oxide bond between strontium and oxygen and the peaks shifted slightly to higher wave number side with increase in the Sr content.

The medium peaks near 1080–1120 cm^{-1} are due to symmetric C—O stretch. All the samples exhibited a similar spectrum with a carbonate peak near 1450–1460 cm^{-1}, which may be due to asymmetric C—O stretch. The C—O stretch may arise due to the chelation and polymerization process resulting in the formation of metal complexes which are not observed as Sr content increased. The C—O bonding region is the indicative of organic content in the material due to the presence of residual oxides. These carbonates may not be detected by XRD because of their existence in amorphous phase in very small fractions. The assignment mode of the
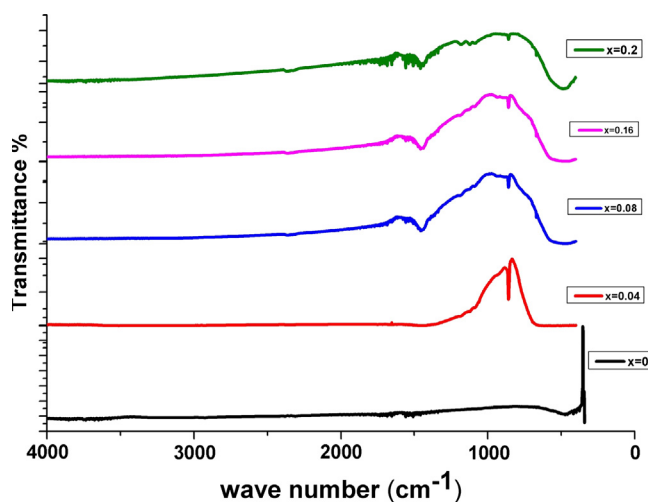
(a)

(b)

(c)

(d)

(e)

Fig. 3   SEM images and EDAX spectra of sintered samples of $Ba_{1-x}Sr_xCe_{0.65}Zr_{0.25}Nd_{0.1}O_{3-\delta}$ for (a) $x = 0$, (b) $x = 0.04$, (c) $x = 0.08$, (d) $x = 0.16$, (e) $x = 0.2$.

bands of sintered powders is reported in Table 3. These values are consistent with the standard IR peaks table [37] and clearly show the complete formation of pure phase.

The increase in the absorption peak shifts to higher energy end with increase in Sr content is expected from a harmonic oscillator model that has been used to stimulate the two body stretching mode.

$$\omega_o = \sqrt{\frac{k}{\mu}} \tag{4}$$

Fig. 4 FTIR spectrum obtained for sintered powders.

where ω_o is the characteristics frequency, k is young's modulus and μ is the effective mass of the oscillator. The effective mass of (Ba-Sr)-O oscillator shrinks as Sr ions substitute Ba ions, due to the lighter atomic weight of Sr, which results in a higher characteristic frequency [38].

Raman spectroscopy

A Raman mapping technique is utilized to examine the local phase distribution of the $Ba_{1-x}Sr_xCe_{0.65}Zr_{0.25}Nd_{0.1}O_{3-\delta}$ oxides in this study as observed from Fig. 5. Denming and Rose [38] proposed that a number of factors contribute to changes of Raman band position including phonon confinement, strain, particle size effect and defects. Differences in particle size led to variation in phonon relaxation and thus causes band shift. The small peak obtained in the range $100-112$ cm^{-1} might be assigned to the stretching mode of the carbonate ion around the Sr ion. The Raman band around $315-325$ cm^{-1} corresponds to $SrCeO_3$ like and $400-440$ cm^{-1} to $ZrCeO_2$ like second phase and are the bending modes of ZrO_6 [39–42]. The small peak near 472 cm^{-1} may be due to

Ce-O-Ce symmetric vibration due to first order scattering that arises due to Nd and the small peaks in the range $552-565$ cm^{-1} might be attributed to the stretching mode of oxygen ion around strontium; $1490-1520$ cm^{-1} may be due to $SrCO_3$ as peaks shifted to higher wavenumber side with increase in concentration of Sr^{2+}. The reason may be due to change in the force constants of the respective bonds and decrease in the effective atomic mass [38,35] which is consistent with XRD that CeO_2 like second phase diminishes with increase in sr^{2+} content.

Impedance measurements

Electrolyte conduction greatly affects the overall energy performance of high temperature solid oxide fuel cells. Here, the ionic conductivity of the $Ba_{1-x}Sr_xCe_{0.65}Zr_{0.25}Nd_{0.1}O_{3-\delta}$ was evaluated as a function of temperature in dry air atmosphere and in wet air. The impedance spectra are measured from room temperature to 500 °C. The temperature was confined to 500 °C due to instrumental limitations and measurements at higher temperature are under process, which will be
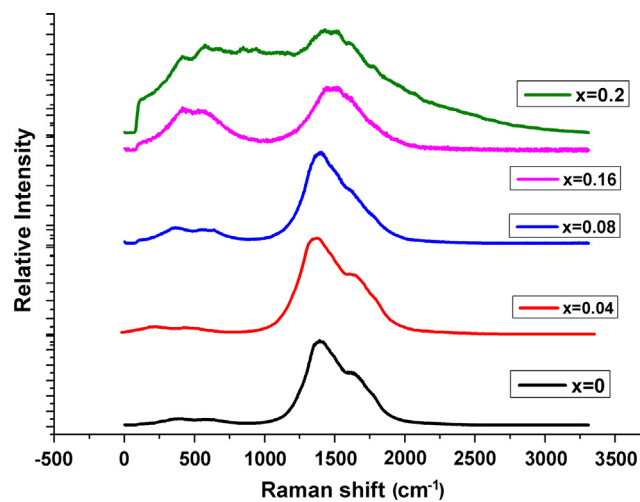

Fig. 5 Raman spectra of sintered samples.

Table 3 Comparison of the grain conductivity (σ_g) and activation energy (E_a) with the reported values.

Compound	Sintering temperature	σ_g (S/cm)	E_a (eV)	Crystallite size (nm)	Ref.
$Ba(Ce_{0.75}Zr_{0.25})_{0.9}Nd_{0.1}O_{2.95}$	1400/5 h	3.7×10^{-5} (300 °C)			[17]
$BaCe_{0.9}Nd_{0.1}O_{2.95}$	1300/5 h	2.4×10^{-3} (800 °C)	0.47 (moist air)		[17]
$Ba_{1-x}Sr_x(Ce_{0.75}Zr_{0.25})_{0.9}Nd_{0.1}O_{2.95}$	1550 °C/24 h		0.57–0.73		[36]
$Ba_{1-x}Sr_xCe_{0.9}Nd_{0.1}O_{2.95}$		0.07×10^{-3} (600 °C) H$_2$ atmosphere			[22]
$BaCe_{0.65}Zr_{0.25}Nd_{0.1}O_{3-\delta}$	1300 °C/5 h	2.08×10^{-3} (500 °C) air 2.12×10^{-3} (500 °C) wet air	0.5	29.1	This work
$Ba_{0.96}Sr_{0.04}Ce_{0.65}Zr_{0.25}Nd_{0.1}O_{3-\delta}$	1300 °C/5 h	1.02×10^{-3} (500 °C) air 1.16×10^{-3} (500 °C) wet air	0.54	29.6	This work
$Ba_{0.92}Sr_{0.08}Ce_{0.65}Zr_{0.25}Nd_{0.1}O_{3-\delta}$	1300 °C/5 h	8.1×10^{-4} (500 °C) air 8.29×10^{-4} (500 °C) wet air	0.55	30	This work
$Ba_{0.84}Sr_{0.16}Ce_{0.65}Zr_{0.25}Nd_{0.1}O_{3-\delta}$	1300 °C/5 h	4.71×10^{-4} (500 °C) air 4.98×10^{-4} (500 °C) wet air	0.58	30.5	This work
$Ba_{0.8}Sr_{0.2}Ce_{0.65}Zr_{0.25}Nd_{0.1}O_{3-\delta}$	1300 °C/5 h	4.62×10^{-4} (500 °C) air 4.83×10^{-4} (500 °C) wet air	0.6	31.3	This work

reported further. The spectra comprise of three arcs at high, medium and low frequencies corresponding to the interior of grain, grain boundary and the electrode respectively [43]. In the Nyquist plots of the present work as observed from Fig. 6a, the high frequency and low frequency arcs are missing due to the instrumental limitations of temperature and frequency. Hence the bulk response was assigned to the high frequency intercept of the medium arc with the real axis which depicted variations of about two to three orders of magnitude with rise in temperature from 30 to 500 °C. The semi-circular pattern represents the electrical process taking place that can be expressed in an electrical circuit with a parallel combination of resistive and capacitive elements.
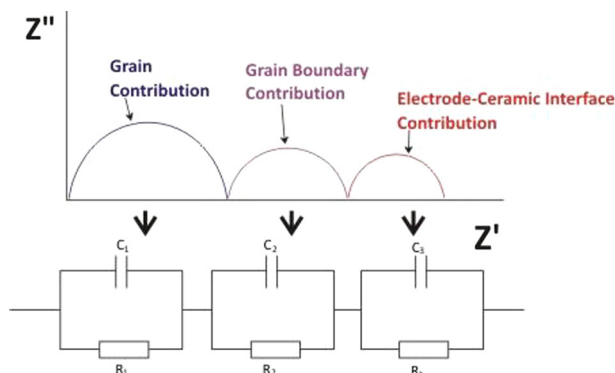
Also the frequency dependent conductivity and dielectric permittivity studies yield important information on the ion transport and relaxation studies of fast ionic conductors. EIS data can be represented in two basic formulas interrelated with each other which are given below.

Complex impedance $Z^* = Z' - jZ''$ (5)

Complex permittivity $\varepsilon^* = \varepsilon' - j\varepsilon''$ (6)

where

C = vacuum capacitance

$\omega = 2\pi f$, angular frequency

Z', ε' = real components of impedance and permittivity

Z'', ε'' = imaginary components of impedance and permittivity

$J = \sqrt{-1}$

The capacitance of any component depends on the relative permeability of the material and on the geometric dimensions of the three frequency regions. The obtained C values of $Ba_{1-x}Sr_xCe_{0.65}Zr_{0.25}Nd_{0.1}O_{3-\delta}$ oxide are found to vary from 10^{-12} F for high frequency arc and conserved this value at 10^{-10} F for low frequency indicating that they corresponds to grain boundary conduction and electrode polarization. The differences observed in C at low temperature may probably be strongly related to the difficulty in the separation of grain and bulk contribution. Declining grain boundary conductivity was attributed to increase in the grain boundaries with reduction in the grain size in addition to structural distortion of the lattice.

Bode plots

Nyquist plots are the first choice for EIS measurement but have a drawback that they do not provide information regard-

ing time or frequency. To avoid this problem Bode plots can be analysed. The variations of real (Z') and imaginary (Z'') parts of impedance with frequency measured at different temperatures of the sample $Ba_{0.8}Sr_{0.2}Ce_{0.65}Zr_{0.25}Nd_{0.1}O_{3-\delta}$ are shown in the Suppl. Fig. 1a. The Z' values decreased sharply with increase in frequency and display characteristic dispersion at low frequencies.

The value of Z'' increased with a rise in frequency followed by a decrease and the peak positions shifted towards higher frequency side along with peak broadening with rising temperatures as shown in Suppl. Fig. 1b of the sample $Ba_{0.8}Sr_{0.2}Ce_{0.65}Zr_{0.25}Nd_{0.1}O_{3-\delta}$. The asymmetric broadening of peaks in Z'' vs. frequency entails that there is a spread of relaxation time, which indicates a temperature dependence electrical relaxation phenomenon in the material [44]. The peak in the lower frequency region may appear due to the electrode polarization.

AC conductivity studies

The electrical conductivity studies of the synthesized compound have been carried out over a frequency range of 20 Hz to 1 MHz with the temperature range of 30–500 °C. The conductivities are found to be ∼10^{-4} S/cm at 500 °C temperature respectively for all the doped samples. The AC conductivity is calculated from dielectric data using the relation:

$$\sigma_{ac} = \omega \varepsilon_r \varepsilon_0 \tan \delta \qquad (7)$$

where $\omega = 2\pi f$

The Arrhenius plots are estimated from the conductivity data using the Arrhenius equation given in eel (8).

$$\sigma_{ac} = \sigma_o \exp\left(\frac{-E_a}{K_b T}\right) \qquad (8)$$

where E_a is the activation energy. The Arrhenius plots obtained from the conductivity data in air and wet atmosphere of all the samples followed a linear trend and higher values of conductivity are observed in humidified air than in dry air as shown in Fig. 6. Oxygen ions are conducted with the aid of oxygen vacancies present in the lattice in which the motion of oxygen vacancies that are considered as the mobile charge carriers gives rise to activation energy.

The variation of the ac conductivity as a function of frequency (from 20 Hz to 1 MHz) clearly demonstrates that the AC conductivity curves show two distinct regions. The first one is the low frequency region in which the conductivity is almost frequency independent and this corresponds to the random hopping of charges. The second one is the high frequency region in which the conductivity increases rapidly and reaches the highest value at 1 MHz, corresponding to frequency dependent conductivity. This behaviour is a characteristic of hopping of charges between the trap levels situated in the band gap. These two types of conductivities are observed in all samples.

The obtained results of all the samples are found to be dependent on the temperature as well as on the concentration of the substituted Sir ions. It was observed that the conductivity of each sample increases with a corresponding increase in temperature, indicating that the electrical conduction in the samples is a thermally activated process. Thus, the observed electrical conductivity was found to occur due to the hopping
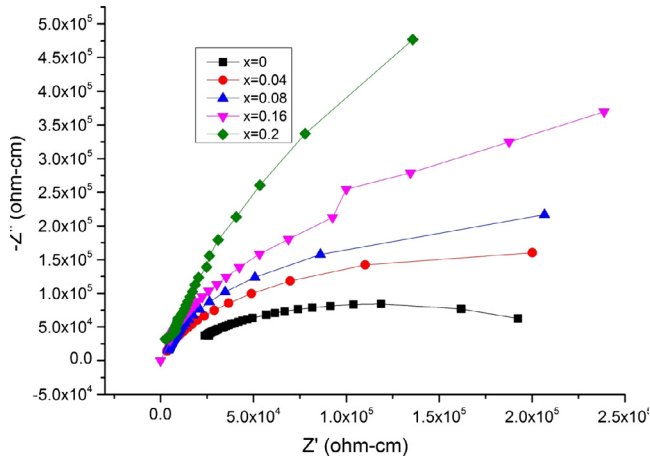
Fig. 6a Nyquist plot sintered $Ba_{1-x}Sr_xCe_{0.65}Zr_{0.25}Y_{0.1}O_{3-\delta}$ pellets at 140 °C.
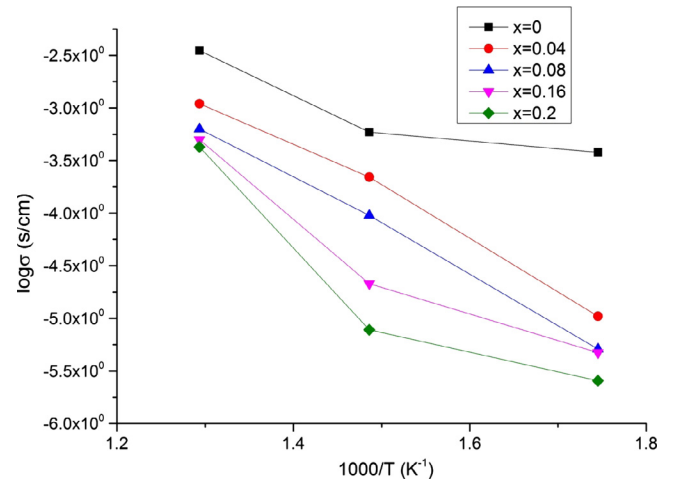

Fig. 6c Arrhenius plot total conductivity of samples sintered in air atmosphere with 3% relative humidity.
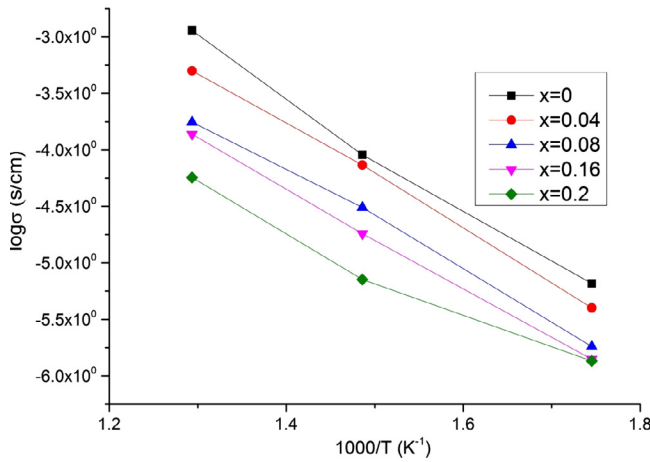

Fig. 6b Arhennius plot total conductivity of samples sintered in air atmosphere.

of small poltroons associated with the behaviour of changeable oxidation state of the metal ions. As the temperature increases, the poltroons have sufficient thermal energy to get activated and jump over the barrier and that is the reason for larger values of conductivity of samples observed at higher temperatures. The conductivity values of $Ba_{0.8}Sr_{0.2}Ce_{0.65}Zr_{0.25}Nd_{0.1}O_{3-\delta}$ are found to be 4.62×10^{-4} S/cm (dry air) and 4.83×10^{-4} S/cm (wet air with 3% relative humidity) at 500 °C and the conductivity depicted an increase in its value with increase in temperature from $\sim10^{-7}$ S/cm at room temperature to $\sim10^{-5}$ S/cm above 300 °C. The increase in conductivity with rise in temperature shows that this composition exhibits ionic conduction. These results are found to be in the range of the electrical conductivity of semiconductor (10^{-3}–10^{-5} S/cm), indicating the semiconductor behaviour of the samples.

A lower conductivity value is observed in dry air than in humid atmosphere due to the absence of water which is necessary to create proton charge carriers to exhibit proton conduction mechanism but the present compound exhibited a

comparable value due to its synthesis process of sol-gel, which resulted in dense structures with more conductivity values at less sintering temperatures. The photonic conductivity of $BaCe_{0.9}Nd_{0.1}O_{2.9}$ reported a value of 2.4×10^{-5} S/cm and $Ba(Ce_{0.75}Zr_{0.25})_{0.9}Nd_{0.1}O_{2.95}$ with 3.7×10^{-5} S/cm at 600 °C [45] and the present value of conductivity obtained for $BaCe_{0.65}Zr_{0.25}Nd_{0.1}O_{3-\delta}$ is 2.08×10^{-3} (500 °C) air and 2.12×10^{-3} at 500 °C (wet air with 3% relative humidity). This is greater than that of the reported values. Among the five samples, the composition without Sir exhibited highest conductivity, which is in agreement with the reported values as shown in Suppl. Fig. 2. A comparison of activation energy and conductivity of the samples with previous results is presented in Table 3.

In wet air atmosphere there are two types of charge carriers, the photonic defects ($OH_o^{\cdot}$) and oxygen vacancies ($V_o^{\cdot\cdot}$). This increases the concentration of charge carriers in the lattice. Hence, the transportation of these charged species (am bipolar diffusion) gives rise to mixed ionic photonic conduction in wet air atmosphere and leads to a conductivity rise [46,30]. In $BaCeO_3$ perovskite, replacement of Ce^{4+} with trivalent Nd^{3+} creates oxygen vacancies which in turn resulted in the formation of photonic defects due to dissociative absorption of water in wet atmosphere represented by KrÖger-Vink notion. The formation of hydroxyl ions with oxygen vacancies initiates on the oxygen ion site for the incorporation of water through the reaction given below.

$$H_2O + V_o^{\cdot\cdot} + O_o^x \iff 2OH_o^{\cdot} \tag{9}$$

The mechanism of proton migration accompanied by series of jumps from one position to another is proposed by Iwahara [47] and further experimented by Kreuer [44]. In the presence of hydrogen, H_2 possibly reacts with oxide ions in the lattice producing electrons and hydroxyl groups given by the reaction.

$$\frac{1}{2}H_2 + O_o^x = OH_o^{\cdot} + e' \tag{10}$$

On further incorporation of Sr and with increase in the concentration of Sr, the grain size decreased. As the grains became smaller in size it resulted in more grain boundary and thereby

has large contact surface of the grains representing barriers to the transport of charged species which in turn raise the activation energy. Also with increase in the amount of Sr, the increase in the free vacancies ceases and further dissolution might took place with the formation of associates and there might be a subsequent decrease in conductivity associated with the amount of free vacancies due to the growth of associate concentration $(R'_{Ce} - V_o^{\cdot\cdot})$ and $(R'_{Ce} - V_o^{\cdot\cdot} - R'_{Ce})^x$.

The activation energy of the sample increased from 0.5 eV with Sr content $x = 0$ to $x = 0.2$ (0.6 eV) which is determined from the slope of the plot Log σ vs. 1000/T and found to be lesser than that of the reported value available in the literature [44]. The parameters such as basicity of the component metal oxides, covalency/ionicity of the M-O bond, polarizability of the cation, and extent of dopant hydroxyl group association also play a prominent role in determining E_σ. The level and type of conductivity of the materials depend on the nature of atoms in the A and B positions of the ABO_3 perovskite structures. Conductivity increased with a decrease in the electro negativity of the A and B elements. The electro negativity values of Sr (0.95) and Nd (1.14) are greater than Ba (0.89) and Ce (1.12) of the A and B sites respectively [36]. As it is known that the conductivity of $SrCeO_3$ is lower than that of $BaCeO_3$, it is evident that doping Sr would reduce conductivity as shown in Suppl. Fig. 2. Furthermore formation of secondary phases, increase in the structural distortion due to decrease in the tolerance factor, increase in the grain boundary resistance due to smaller grain size and higher electro negativity may be responsible for the increase in the energy barrier, which in turn increased activation energy and held responsible for the decrease in the electrical conductivity value.

Dielectric constant (ε')

The variation of Dielectric constant with temperature (200–500 °C) and frequency (20 Hz to 10^6 Hz) is studied. From the frequency dependent plot of the sample $Ba_{0.8}Sr_{0.2}Ce_{0.65}Zr_{0.25}Nd_{0.1}O_{3-d}$, it was observed that the value of e' decreases sharply with the increment in the values of frequency (Suppl. Fig. 3a). For the sample $Ba_{0.8}Sr_{0.2}Ce_{0.65}Zr_{0.25}Nd_{0.1}O_{3-\delta}$, it was observed that the value of ε' decreases sharply with the increment in the values of frequency. All the samples reported the same trend and hence are not represented here. The higher values of dielectric constant at low frequencies can be due to space charge polarization (power frequencies) which occurs due to accumulation of charges at the interfaces in between the electrode and the sample. In low frequency regions the dipoles get adequate time to orient themselves completely along the field direction when an alternating field is applied on the sample, resulting in larger values of ε' of the samples. As the frequency increases further, the dipoles in the samples cannot reorient themselves fast enough in response to the applied electric field but lag behind, resulting in the decrease in ε' and reaching a constant value pertaining to higher frequencies applied to the sample up to 10^6 Hz.

Suppl. Fig. 3b. represents the variation of imaginary part of dielectric permittivity (ε'') with frequency of the sample at different temperatures and the graph showed a decrease in the (ε'') values ascending the frequency for $x = 0.2$. The higher values at lower frequency may be due to free motion of charge carriers within the material and as the frequency increases dielectric

loss increases, which reflects in a decrease in the value of the dielectric permittivity.

From the plot of dielectric constant versus temperature as represented by Suppl. Fig. 3, it is observed that as temperature rises, an increase is observed in the dielectric constant. This can be explained as follows. In space charge polarization, diffusion of ions takes place with a rise in temperature. Additionally, thermal energy may also assist in overcoming the activation barrier for the orientation of polar molecules in the direction of the field which increases the value of ε'.

Dielectric loss tangent (tan δ)

In the presence of an alternating field, dipoles align in the direction of field and as time passes by, with the change in the field they rotate again. In the process of alignment energy is lost and a local heat is generated in which the dielectric loss is given by loss tangent (tan δ). Suppl. Fig. 4 represents the variation of Tan δ vs. logf at different temperatures. Space charge polarization at grain boundaries (low frequency peak) and dipolar rotations associated with the bulk (high frequency peak) may be responsible for the loss [30,36,47–49]. With increase in the temperature, diffusion of thermally activated protons takes place from grains to grain boundaries that result in the decrease in the space charge polarization. The degree to which the dipole is out of phase with the applied field and the losses that develop determine how large the imaginary part of permittivity depends on the material properties and applied frequency. The larger the imaginary part, the more will be the energy dissipated through motion and less is available for propagation through the dipole. Thus imaginary part of relative permittivity (ε'') has a direct relation to loss in the system.

Low temperature SOFCs operating lower than 650 °C are gaining present attention owing to the reason that decreased operating temperatures can attain maximum theoretical efficiency of the fuel cell. Low temperature SOFCs are only possible with higher conducting electrolytes. The conductivity of BCNY electrolyte was reported to be 4.1×10^{-3} S/cm at 973 K with a fuel cell performance of $200–300 \times 10^6$ W/cm^2 [50]. Also pure proton conductivity was displayed by $Ba_{0.5}Sr_{0.5}Ce_{0.6}Zr_{0.2}Gd_{0.1}Y_{0.1}O_{3-\delta}$ (1×10^{-2} S/cm in wet H_2) with an open circuit voltage of 1.15V/H_2 air [51]. $BaCe_{0.7}In_{0.1}Gd_{0.2}O_{3-\delta}$ reported a higher conductivity value of 1×10^{-2} S/cm at 832/k in air atmosphere which is sintered at 1700 °C for 10 h has been considered as an alternative electrolyte for SOFC [52]. From the above stated literature it is evident the present compositions attained a comparable conductivity values at a lower sintering temperatures (1300 °C) which can be beneficial for the increase in the fuel cell efficiency which are under further study. As expected Neodymium incorporation into the lattice increased conductivity while doping Sir into the A sites increased chemical stability and hence this composition can be a promising electrolyte if all the values such as sintering temperature, dopant concentration and time are proportionally controlled. An overview of the literature available with the present values of conductivity is represented in Table 3.

Conclusions

This study has systematically presented the relationship between Sir doping content and microstructure, chemical sta-

bility and conductivity of $Ba_{1-x}Sr_xCe_{0.65}Zr_{0.25}Nd_{0.1}O_{3-\delta}$ ($0 \leqslant x \leqslant 0.2$) electrolyte prepared by sol-gel method. Single phase perovskite nanostructured $Ba_{1-x}Sr_xCe_{0.65}Zr_{0.25}Nd_{0.1}O_{3-\delta}$ powders are obtained by a modified sol-gel pechini process. The lattice constants and unit cell volumes are found to decrease as Sr atomic percentage increased in accordance with the Vegard law, confirming the formation of Solid Solution. Incorporation of Sr into the composition resulted in smaller grains besides suppressing the formation of $SrCeO_3$ same as second phase. Among the synthesized samples $BaCe_{0.65}Zr_{0.25}Nd_{0.1}O_{3-\delta}$ pellet with orthorhombic structure showed the highest conductivity with a value of 2.08×10^{-3} S/cm (dry air) and 2.12×10^{-3} S/cm (wet air with 3% relative humidity) at 500 °C due to its smaller lattice volume, larger grain size and lower activation energy that led to excessive increase in conductivity. $Ba_{0.8}Sr_{0.2}Ce_{0.65}Zr_{0.25}Nd_{0.1}O_{3-\delta}$ recorded lower conductivity with a value of 4.62×10^{-4} S/cm (dry air) and 4.83×10^{-4} S/cm (wet air with 3% relative humidity) at 500 °C. All pellets exhibited good chemical stability when exposed to air and H_2O atmospheres. Comparisons with the literature showed the importance of the synthesis method on the properties of the powders. As expected Neodymium incorporation into the lattice increased conductivity while doping Sr into the A sites increased chemical stability and hence this composition can be a promising electrolyte if Sr addition is limited to small amounts.

Conflict of Interest

The authors have declared no conflict of interest.

Compliance with Ethics Requirements

This article does not contain any studies with human or animal subjects.

Acknowledgements

Appendix A. Supplementary material

Supplementary data associated with this article can be found, in the online version, at http://dx.doi.org/10.1016/j.jare.2016.12.006.

References

[1] Haile SM, Staneff G, Ryu KH. Non-stoichiometry, grain boundary transport and chemical stability of proton conducting perovskites. J Mater Sci 2001;36:1149–60.

[2] Hermet J, Bottin F, Dezanneau G, Geneste G. Hydrogen diffusion in the protonic conductor $BaCe_{1-x}Gd_xO_{3-x/2}$ from density functional theory. Phys Rev B 2012;87:104303.

[3] Tania P, Kanwar Gulsher Singh P, Thangadurai V. Perovskite type metal oxides exhibiting negligible grain boundary resistance to total electrical conductivity. Inorg Chem 2008;47:8972–84.

[4] Zhao F, Liu Q, Wang S, Brinkman K, Chen F. Synthesis and characterisation of $BaIn_{0.3-x}Y_xCe_{0.7}O_{3-\delta}$ (x = 0,0.1,0.2,0.3) proton conductors. Int J Hydrogen Energy 2010;35:4258–63.

[5] Zhao F, Chen F. Performance of solid oxide fuel cells based on proton-conducting $BaCe_{0.7}In_{0.3-x}Y_xO_{3-\delta}$ electrolyte. Int J Hydrogen Energy 2010;35:11194–9.

[6] Iwahara H. Proton conducting ceramics and their applications. Solid State Ion 1996;86–88:9–15.

[7] Ivanov MG, Shmakov AN, Drebushchak VA, Podyacheva Oyu. Two mechanisms of thermal expansion in perovskite $SrCo0.6Fe0.2Nb0.2O3-z$. J Therm Anal Calorim 2010;100:79–82.

[8] Tong J, Clark D, Bernau L, Subramaniyan A, Hayre OR. Proton-conducting yttrium-doped barium cerate ceramics synthesized by a cost-effective solid-state reactive sintering method. Solid state Ion 2010;181:1468–98.

[9] Bi L, Tao Z, Liu C, Sun W, Wang H, Liu W. Fabrication and characterisation of easily sintered and stable anode supported proton conducting membranes. J Memb Sci 2009;336:1–6.

[10] Zhahriev A, Kaloyanov N, Girginov C, Paranova V. Synthesis and thermal decomposition of $[Bi_6O_6(OH)_{(2)}](NH_2C_6H_4SO_3)_{(4)}$. Thermochim Acta 2012;528:85–9.

[11] Iwahara H, Uchidda H, Morimoto K. High temperature solid electrolyte fuel cells using perovskite- type oxide based on $BaCeO_3$. J Electrochem Soc 1990;137:462.

[12] Bonanos N, Ellis B, Mohmood M. Construction and operation of fuel cells based on solid electrolyte $BaCeO_3$:Gd. Solid State Ion 1991;44:305.

[13] Ryu KH, Haile SM. Chemical stability and proton conductivity of doped $BaCeO_3$-$BaZrO_3$ solid solutions. Solid State Ion 1999;125:355–67.

[14] Amini MM, Mirzaee M. Effect of solvent and temperature on the preparation of potassium niobate by hydrothermal-assisted sol–gel processing. Ceram Int 2009;35:2367–72.

[15] Cetvera RB, Oyama Y, Yamaguchi S. Low temperature synthesis of a crystalline proton conducting $BaZr_{0.8}Y_{0.2}O_3$ by sol-gel method. Solid state Ion 2007;178:569–74.

[16] Kreuer KD. On the development of proton conducting materials for technological applications. Solid state Ion 1997;97:1–15.

[17] Kwang HR, Haile SM. Chemical stability and proton conductivity of $BaCeO_3$-$BaZrO_3$. Solid State Ion 1999;125:355–67.

[18] Fanglin C, Ping W, Sorensen OT, Meng G, Peng D. Preparation of Nd doped $BaCeO_3$ proton conducting ceramics by homogenous oxalate co-precipitation. J Mater Chem 1997;7(15):33–1539.

[19] Su XT, Yan QZ, Max XH, Zhang WF, Ge CC. Effect of codopant addition on the properties of yttrium and neodymium doped barium cerate electrolyte. Solid State Ion 2006;177(11–12):1041–5.

[20] Lee YC, Hung IM, Chang SL, Ciou CJ, Wu JS. The effects of doped Nd on conductivity and phase stability of $BaCe_{0.8}Y_{0.2}O_{3-\delta}$ based electrolyte for solid oxide fuel cell. J Eur Ceram Soc 2011;31(16):3137–43.

[21] Fu XZ, Luo JL, Sanger AR, Danilovic N, Chuang KT. Au integral proton conducting SOFC for simultaneous production. Chem Commun 2010;46(12), 2052-2.

[22] Zhang C, Zhao H. Electrical conduction behaviour of Sr substituted proton conductor $Ba_{1-x}Sr_xCe_{0.9}Nd_{0.1}O_{3-\delta}$. Solid State Ion 2010;181(33-34):1478–85.

[23] Iwahara H. Technological challenges in the application of proton conducting ceramics. Solid State Ion 1995;77:289–98.

[24] Cai M, Liu S, Efimov K, Caro J, Wang H. Preparation and hydrogen permeation of $BaCe_{0.95}Nd_{0.05}O_{3-\delta}$ membranes. J Membr Sci 2009;343(1-2):90–6.

[25] Taniguchi N, Kuroha T, Nishimura C, Iijima K. Characteristics of novel $BaZr_{0.4}Ce_{0.4}In_{0.2}O_3$ proton conducting ceramics and their application to hydrogen sensors. Solid State Ion 2005;176 (39-40):2979–83.

[26] Wienstroer S, WiemhÖffer H. Investigation on the influence of zirconium substitution on the properties of Neodymium doped barium cerates. Solid State Ion 1997;1113:101–3.

[27] Scholten M, Schoonman J, Van Miltenberg JC, Oonk HAJ. Synthesis of strontium and Barium Cerate and their reaction with carbon dioxide. Solid State Ion 1993;61:83.

[28] Li ZhiJie, Liu RuiQuan, Wang JiDe, Zheng Xu, Xie YaHong, Wang BenHui. Preparation of double doped $BaCeO_3$ and its application in the synthesis of ammonia at atmospheric pressure Sci Technol. Adv Mater 2007;8:566–70.

[29] Babu AS, Bauri Ranjit. Synthesis phase stability and conduction behaviour of rare earth and transition metals doped barium cerates. Int J Hydrogen Energy 2014;39:14487–95.

[30] Chen F, Sorensen OT, Meng G, Peng D. Preparation of Nd doped Barium Cerates through different routes. Solid State Ion 1997;10:63.

[31] Zeng Y, Mao PL, Jiang SP, Zhang L, Wu P. Prediction of Oxygen ion conduction from relative coulomb electronic interactions in Oxya patites. J Power Sources 2011;196:4524–32.

[32] Wang S, Zhao F, Zhang L, Brinkman K, Chen F. Stability and electrical property of $Ba_{1-x}Sr_xCe_{0.8}Y_{0.2}O_{3-\delta}$ high temperature proton conductor. J Alloys Compd 2010;506:263–7.

[33] Lu JD, Wang L, Fan LH, Li H, Dai L. H X Guo. Chemical stability of doped $BaCeO_3$-$BaZrO_3$ solid solutions in different atmospheres. J Rare Earth 2008;26:505–10.

[34] Matsumoto H, Kawasaki Y, Ito N, Enoki M, Ishihava T. Relation between electrical conductivity and chemical stability of $BaCeO_3$-based proton conductors with different trivalent dopants. Electrochem Solid State Lett 2007;10:77–80.

[35] Kan-Rong Lee, Chia-Tzu Chenb, Chung-Jen Tsengb, Changa Jeng-Kuei, I-Ming Hungc, Jing-Chie Lina, et al. Strontium doping effect on phase homogeneity and conductivity of $Ba_{1-x}Sr_xCe_{0.6}Zr_{0.2}Y_{0.2}O_{3-\delta}$ solid oxide fuel cell electrolytes. Int J Hydrogen Energy 2013:11097–103.

[36] Zajac W, Hanc E. Strontium substituted $BaCeZrO_{3-\delta}$ oxides for proton conducting membranes. Funct Mater Lett 2014;7:1440014–17.

[37] Osman N, Ibrahim AT, Hamidi AH. Preparation and characterization of Yb doped $Ba(CeZr)O_3$ nanopowders with high sinterability. Ionics 2010;16:561–9.

[38] Denming JH, Rose SD. The vibrational spectra and structures of rare earth oxides in the A site modification. J Phys C: Solid State Phys 1972;15:1123–33.

[39] Long RQ, Haung YP, Wan HLJ. Surface oxygen species over cerium oxide and their reactivities with methane and ethane by means of in situ confocal microprobe Raman spectroscopy. J Raman Spectrosc 1997;28:29–32.

[40] Okoyama Y, Isa K, Sung Lee Y, Takaaki Sakai. Incorporation and conduction of proton in $SrCe_{0.9-x}Zr_xY_{0.1}O_{3-\delta}$. Solid State Ion 2015;275:35–8.

[41] Kim BK, Hamaguxchi HO. Mode assignments of the Raman spectrum of monoclinic zirconia by isotopic exchange technique. Phys Status Solidi B 1997;203:557–63.

[42] Genet F, Loridant S, Ritter C, Lacazeau G. Phase transitions in $BaCeO_3$:neutron diffraction and Raman studies. J Phys Chem Solids 1999;60:2009–21.

[43] Yashiro K, Suzuki T, Kaimai A, Matsumoto H, Nigara Y, Kawada T. Electrical properties and defect structure of Niobia doped ceria. Solid State Ion 2004;175(1-4):341–4.

[44] Kreuer KD. On the development of proton conducting materials for technological applications. Solid State Ion 1997;97:1–15.

[45] Zając W, Hanc E, Gorzkowska-Sobas A, Swierczek K, Molenda J. Nd-doped $Ba(CeZr)O_{3-\delta}$ proton conductors for application in conversion of CO_2 into liquid fuels. Solid State Ion 2012;225:297–303.

[46] Yamazaki Y, Hernandz-Sanchez R, Haile SM. Cation non-stoichiometry in yttrium-doped barium zirconate: phase behaviour, microstructure, and proton conductivity. J Mater Chem 2010;81:58–66.

[47] Iwahara H, Asakura Y, Katahira K, Tanaka M. Prospect of hydrogen technology using proton conducting ceramics. Solid State Ion 2004;168:299–310.

[48] Youminguo, Ran R, Shao Z. Optimizing the modification method of zinc-enhanced sintering of $BaZr_{0.4}Ce_{0.4}Y_{0.2}O_{3-\delta}$-based electrolytes for application in an anode-supported protonic solid oxide fuel cell. Int J Hydrogen Energy 2010;35:5611–20.

[49] Jung KW, Yang DC, CN, Park CJ, Choi J. Effects of the addition of ZnO and Y_2O_3 on the electrochemical characteristics of a $Ni(OH)_2$ electrode in nickel–metal hydride secondary batteries. Int J Hydrogen Energy 2010; 35: 13073–77.

[50] Zetian T, Quinfang Z, Xinguo X, Guihua H, Lei B. A strategy of tailoring stable electrolyte material for high performance proton conducting solid oxide fuel cells (SOFCS). Electrochem Commun 2016;72:19–22.

[51] Ramaiyan K, Kalpana S, Sukhdeep G, Tobias F, Venkatraman T. Chemically stable proton conducting doped $BaCeO_3$-no more fear to SOFC wastes. Sci Rep 2013;3:2138–42.

[52] Xiao ML, Zhan GL, JiaH O, Yi JG, Jun X, Fu YY. Structure and electrical conductivity of $BaCe0.7In0.1A0.2O3-\delta$ (A = GD, Y) ceramics. Electrochim Acta 2012;59:464–9.